



Dual interface-reinforced built-in electric field for chlorine-free seawater oxidation

Shucong Zhang, Yan Wang, Xiaotong Wei, Lei Chu, Weiqian Tian, Huanlei Wang, Minghua Huang^{*}

School of Materials Science and Engineering, Ocean University of China, Qingdao 266100, PR China

ARTICLE INFO

Keywords:

Dual-interface engineering
Chlorine-free
Built-in electric field
Seawater oxidation
High current density

ABSTRACT

It is imperative but challenging for the development of oxygen evolution reaction (OER) catalysts suitable for high-current density seawater electrolysis without detrimental chlorine chemistry. Herein, we report a (Ni, Fe) OOH@Ni_xP heterogeneous catalyst comprising the (Ni, Fe)OOH/Ni₁₂P₅/Ni₂P dual-interface, in which the Ni₁₂P₅/Ni₂P interface can enhance intrinsic driving force to propel the interfacial electron transport and form a strong built-in electric field (BEF) with asymmetric charge distribution at the (Ni, Fe)OOH/Ni₁₂P₅ interface, simultaneously promoting the OER kinetics and weakening the Cl⁻ adsorption ability. As a result, the (Ni, Fe) OOH@Ni_xP catalyst requires ultralow overpotential of 318 mV to achieve the current density of 500 mAcm⁻² with outstanding stability in alkaline seawater. Notably, almost no hypochlorite is detected in the lab-scale seawater electrolyzer even if the cell voltage exceeds 1.72 V for a long term. This work highlights a design principle for heterogeneous catalysts and makes an important step forward for industrial seawater electrolysis.

1. Introduction

Seawater electrolysis, containing the cathodic hydrogen evolution reaction (HER) and anodic oxygen evolution reaction (OER), has been widely regarded as an appealing and sustainable strategy to simultaneously resolve the issues raised from the energy crisis and freshwater shortage [1]. However, the complex ionic chemistry in seawater electrolysis would lead to the extra challenges, where the dissolved ions in seawater may accelerate degradation of the catalyst materials through the ionic poison and corrosion [2]. Particularly, the chlorine electro-oxidation reaction (ClOR), as a competitor for OER, could generate corrosive chlorine species (e.g., Cl₂, ClO⁻) and thus reduce the electrolysis efficiency and stability [3]. Peter Strasser proposed that the ClOR could be efficiently suppressed by controlling the OER overpotential lower than 490 mV in alkaline seawater [2]. Once the overpotential exceeds 490 mV, it is possible that the OER and ClOR could simultaneously happen due to partially shared reaction pathways or the similar active sites required for these two reactions [4]. In this case, the catalyst material would be seriously corroded by the as-formed chlorine species. Meanwhile, the obtained current density under such limited overpotential is still far from the demand of industry [5]. Therefore, developing OER-preferred catalysts suitable for chlorine-free seawater

electrolysis at high-current density is urgently demanded, but remaining challenges.

It is well known that the OER is a multistep process on the surface of catalysts, involving oxygen intermediates adsorption as well as electron transfer between intermediates and active sites [6,7]. Therefore, the following features should be met for the superior OER catalysts in seawater: i) the intrinsically excellent activity; ii) the abundant active sites; iii) the fast electron and mass transfer ability; iv) the outstanding chemical stability and chlorine resistance [8]. Recently, the coupling of Ni/Fe (oxy)hydroxides with other transition metal compounds through interface engineering, such as NiFeOOH@FeNi [9], NiOOH/Ni₅P₄ [10], Ni₂P/FeOOH [11], NiFe(OH)_x/FeS [12], and Ni₃S₂@NiFeOOH [13] have been considered as a promising tactics for designing efficient catalysts toward OER in seawater. The artificial interface, assembled by above two components with different energy levels, can create spontaneous built-in electric field (BEF) by intelligently achieving asymmetric charge redistribution to optimize the oxygen intermediates adsorption [14–16]. Thereinto, transition metal phosphides (TMPs) have been widely used as promising components to produce such heterogeneous interface [17,18]. They not only possess the high electrical conductivity for improving the electron transport of catalyst systems, but also have intrinsic phosphorus atoms that can be oxidized into phosphates to

^{*} Corresponding author.

E-mail address: huangminghua@ouc.edu.cn (M. Huang).

protect catalyst from chlorine corrosion [19–21]. However, most reports have mainly focused on the construction of Ni/Fe (oxy)hydroxides/TMPs single-interface, in which the weak interaction between such two components can hardly propel the powerful and continuities electron migration at interface for limited tuning of surface charge states, leading to the unsatisfactory catalytic OER performance [22]. It is reported that electron transport capacity at the interface is dominated by the work function (WF) difference, which highly related with the composition and configuration of heterointerface [23]. Therefore, it is feasible and advanced to achieve the targeted optimization of oxygen intermediates adsorption by elaborately constructing and rationally adjusting the interfacial structure to build a relatively powerful BEF.

Dual-interface construction has been either proposed or demonstrated to be capable of improving the intrinsic activity of electrocatalysts [24,25]. Typically, the promising characters of electronic interaction between differentiated interfaces could satisfy the bidirectional enhancement of activity and functionality [26]. In this regard, it is expected to synergistically resolve intrinsic property and chlorine issues in seawater oxidation by realizing a well-managed dual-interface structure. Herein, Ni/Fe (oxy)hydroxides nanoparticles and heterogeneous Ni phosphide nanorod array have been successfully constructed on Ni foam [named as (Ni, Fe)OOH@Ni_xP] via a simple two-step phosphorization-electrodeposition strategy. A dual-interface of (Ni, Fe)OOH/Ni₁₂P₅/Ni₂P is well-integrated in the designed catalyst model, which exhibits the excellent OER performance in alkaline seawater at high current density. To be specific, it only requires the ultralow overpotentials of 278 and 318 mV to arrive a current density of 500 mA cm⁻² in alkaline simulated seawater (1 M KOH+0.5 M NaCl) and alkaline natural seawater (1 M KOH+natural seawater) with outstanding long-term stability for nearly 100 h, respectively. During stability test, almost no generated hypochlorite has been detected in the electrolyte even if the applied potential completely satisfies theoretical value (≥ 1.72 V) required for activating the ClOR. The impressive OER activity is attributed to synergistic collaboration of (Ni, Fe)OOH/Ni₁₂P₅ and Ni₁₂P₅/Ni₂P dual-interface, in which the former (Ni, Fe)OOH/Ni₁₂P₅ provides spontaneous BEF with asymmetric charge distribution at interface for oxygen intermediates adsorption, and the latter Ni₁₂P₅/Ni₂P could further boost this interfacial charge redistribution and reinforce the BEF for optimizing the adsorption free energy. In addition, the well-designed (Ni, Fe)OOH/Ni₁₂P₅/Ni₂P dual-interface also plays a crucial role in decreasing the Cl⁻ adsorption, and thus has a profound impact on the chlorine-free seawater oxidation. This work provides a new perspective for designing the heterogeneous catalysts and stimulates the advancement of the efficient and stable seawater electrolysis at high current density.

2. Experimental section

2.1. Preparation of the catalysts

The (Ni, Fe)OOH@Ni_xP is prepared through a phosphorization-electrodeposition process of the NF substrate. Prior to synthesis treatment, the NF with a size of 1 × 2 cm² is successively placed in absolute ethanol and deionized (DI) water for ultrasonic cleaning of 10 min to remove the surface impurities, followed by drying at 50 °C for 6 h. For the phosphorization procedure, the NaH₂PO₂ and cleaned NF are placed in a ceramic boat and then put into a quartz tube furnace, where the NaH₂PO₂ as phosphorus source and NF as Ni source are located at the upstream and downstream side, respectively. The phosphorization temperature is carried out at 350 °C to get Ni_xP for 1 h with a heating rate of 2 °C min⁻¹ under Ar atmosphere. After being naturally cooled down to ambient temperature, the Ni_xP is taken out carefully and cleaned by ultrasonication in DI water. A standard three-electrode cell, involving the Ni_xP as working electrode, a carbon rod as counter electrode, and Ag/AgCl as reference electrode, is adopted in 50 mL mixed aqueous solution of 0.3 mM Ni(NO₃)₂·6 H₂O and 0.1 mM Fe(NO₃)₃·9

H₂O. The electrodeposition process is then performed under the constant potential of -2 V for 1500 s with a stirring rate of 100 rpm. The final (Ni, Fe)OOH@Ni_xP catalyst is obtained after being washed slowly with DI water and dried naturally in the air. For synthesizing pure (Ni, Fe)OOH catalysts, the NF is directly subjected to the electrodeposition without phosphorization procedure.

2.2. Physical characterizations

The composition of the catalysts is confirmed by the X-ray diffraction (XRD, Bruker D8 Advance diffractometer) with a Cu K α radiation source ($\lambda = 1.54178$ Å). The surface composition and the chemical states for catalysts are further analyzed by the X-ray photoelectron spectroscopy (XPS, Thermo Scientific Escalab 250Xi spectrometer). The UV-visible diffuse reflectance spectra (UV-vis) were measured with a U-4100 Spectrophotometer. The scanning electron microscopy (SEM) measurements of the catalysts are performed by utilizing the Hitachi S-4800 field emission electron microscope. The transmission electron microscopy (TEM), high-resolution transmission electron microscopy (HRTEM) and energy-dispersive X-ray spectroscopy (EDS) are carried out on a FEI Tecnai 20 operated at an accelerating voltage of 200 kV.

2.3. Electrochemical measurements

All electrochemical performances of the as-prepared catalysts are conducted with a CHI 760E electrochemical workstation (Shanghai, China) at room temperature (~25 °C). A standard three-electrode configuration has been carried out for the electrochemical measurements, in which the as-fabricated catalysts are served directly as the working electrodes without any further processing, a graphite rod and the Hg/HgO are served as the auxiliary electrode and the reference electrode, respectively. The OER performance is measured in three different kinds of electrolyte solutions, involving 1 M KOH, alkaline simulated seawater (1 M KOH+0.5 M NaCl), and alkaline natural seawater (1 M KOH+seawater). The seawater is obtained from the Yellow Sea of China and the pH value is around 8.5 after simple filtration. The linear sweep voltammetry (LSV) is carried out with iR compensation at a scan rate of 5 mV s⁻¹. All the potentials applied are calibrated to reversible hydrogen electrode (RHE) according to the following equation: $E_{RHE} = E_{Hg/HgO} + 0.0591 \times \text{pH} + 0.098$. Tafel slope is calculated by using this equation $\eta = a + \log(j)$ to fit the LSV. To evaluate the electrochemical double-layer capacitance (C_{dl}), cyclic voltammetry (CV) is carried out with different scan rates of 20, 40, 60, 80, 100, and 120 mV s⁻¹ in an obvious non-faradaic interval. The electrochemical impedance spectroscopy (EIS) measurement is conducted with 10 mV amplitude in the frequency from 0.01 Hz to 100 kHz. For the stability test, 2000 CV cycles are performed with the scan rate at 100 mV s⁻¹ between 0.2 and 0.6 V.

2.4. Computational methods

All the DFT calculations was carried out in the Vienna ab initio simulation (VASP5.4.4) code. The exchange-correlation is simulated with PBE functional, and the ion-electron interactions were described by the PAW method. The vdWs interaction was included by using empirical DFT-D3 method. Atoms in the upper two layers of the surface are allowed to move freely while the bottom two layers are fixed to simulate the surface of structure. The Monkhorst-Pack-grid-mesh-based Brillouin zone k-points are set as 2 × 2 × 1 for all periodic structure with the cutoff energy of 450 eV. The convergence criteria are set as 0.01 eV Å⁻¹ and 10⁻⁵ eV in force and energy, respectively. The OER process were analyzed by calculating the reaction free energies of all elementary steps along the reaction coordinates, including (i) the hydroxide ion dissociates into OH groups adsorbed on the catalyst surface (*OH); (ii) *OH further reacts with hydroxide ions to dissociate into O groups (*O), and generates water molecules; (iii) *O reacts with a hydroxide ion and

produces an OOH group (*OOH); (iv) eventually O₂ is produced and then released. The free energy calculation of species adsorption (ΔG) is based on following model: $\Delta G = \Delta E + \Delta E_{\text{ZPE}} + \Delta H_{0 \rightarrow T} - T\Delta S$. Herein ΔE , ΔE_{ZPE} , and ΔS respectively represent the changes of electronic energy, zero-point energy, and entropy that caused by adsorption of intermediate. The $\Delta H_{0 \rightarrow T}$ refers to the change in enthalpy when heating from 0 K to T K. The entropy of H⁺+e⁻ pair is approximately regarded as half of H₂ entropy in standard condition.

3. Results and discussion

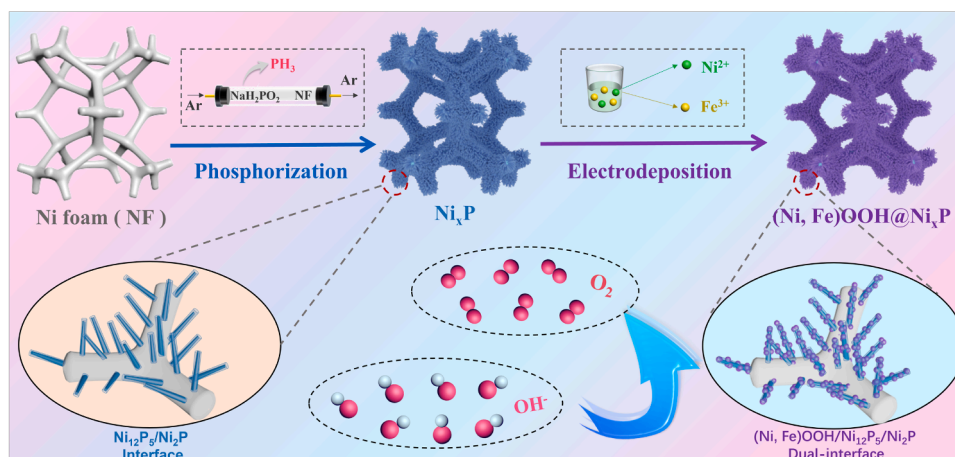
3.1. Synthesis and characterization

Scheme 1 presents the synthesis process of the (Ni, Fe)OOH@Ni_xP catalyst comprising (Ni, Fe)OOH/Ni₁₂P₅/Ni₂P dual-interface. Specifically, the heterogeneous Ni_xP nanorods containing of Ni₁₂P₅/Ni₂P interface are first grown on the NF by utilizing the low-temperature phosphorization method, where the NF and sodium hypophosphite (NaH₂PO₂) are employed as the nickel and phosphorous sources, respectively. The (Ni, Fe)OOH/Ni₁₂P₅ interface is subsequently obtained by electrodepositing amorphous Ni/Fe (oxy)hydroxide nanoparticles onto the surface of the heterogeneous Ni_xP nanorods. With the process of above synthesis, the color of the silver-gray NF substrate gradually changes into black (Fig. S1). For comparison, the pure (Ni, Fe)OOH nanoparticles and pure Ni_xP nanorods on the NF by employing the similar way as for the (Ni, Fe)OOH@Ni_xP catalyst, respectively.

The X-ray diffraction (XRD), scanning electron microscopy (SEM), and transmission electron microscopy (TEM) measurements are conducted to explore the composition and morphology of the (Ni, Fe)OOH@Ni_xP, (Ni, Fe)OOH and Ni_xP. As shown in Fig. 1a, the main characteristic peaks at 38.4, 40.8, 44.6, 46.9, 47.3, and 48.9° for the pure Ni_xP are well indexed to the Ni₂P (PDF#03-0953) and Ni₁₂P₅ (PDF#22-1190). The XRD pattern of the pure (Ni, Fe)OOH shows no peaks, suggesting its amorphous nature (Fig. S2). The peaks of the target (Ni, Fe)OOH@Ni_xP are similar to those of the pure Ni_xP, while no peaks corresponding to (Ni, Fe)OOH can be observed, implying the (Ni, Fe)OOH grown on the Ni_xP are also in the form of an amorphous architecture. As shown in the SEM image of pure Ni_xP (Fig. S3a and S3b), the surface of the NF skeleton is completely covered by vertically grown and well-arranged nanorod arrays. The SEM and TEM images of pure (Ni, Fe)OOH in Fig. S3-f presents that the numerous nanoparticles with an average diameter of 10–20 nm are attached to the NF surface. For the (Ni, Fe)OOH@Ni_xP (Fig. 1b and c), the surface of Ni_xP nanorod arrays are consistently decorated with a large number of (Ni, Fe)OOH nanoparticles. TEM image of the (Ni, Fe)OOH@Ni_xP shows the interface between Ni_xP nanorods and (Ni, Fe)OOH nanoparticles (Fig. 1d),

suggesting successful fabrication of the (Ni, Fe)OOH@Ni_xP hetero-structure. The detailed structure information of the (Ni, Fe)OOH@Ni_xP is further provided by the high-resolution TEM (HRTEM, Fig. 1e). Interestingly, the apparent crystalline/crystalline boundaries between the Ni₂P and the Ni₁₂P₅ can be observed in the Ni_xP nanorods (labeled with short blue dash line). As revealed in Fig. 1f, the clearly visible lattice fringe is separated by the interplanar spacing of 1.926 Å, which can be unambiguously ascribed to the (210) crystal plane of Ni₂P. The distinguishable lattice fringes can also be seen with the interplanar distance of 1.852 and 1.985 Å, which are indexed to (312) and (420) planes of Ni₁₂P₅, respectively. The growth mechanism of Ni₂P/Ni₁₂P₅ interface has been preliminarily discussed in Fig. S4, and such close-coupled interface may act an electron transfer channel to improve the conductivity of catalysts during reaction process. Also, the crystalline/amorphous boundaries can be captured between the (Ni, Fe)OOH and the Ni₁₂P₅ (marked with yellow short dash line), which could provide sufficient electron supply and reaction places to boost the catalytic performance [27,28]. According to the selected area electron diffraction (SAED) pattern, the bright spots correspond to the crystal planes of Ni₂P and Ni₁₂P₅ phases, and the presence of bright rings imply the amorphous state of the (Ni, Fe)OOH phase. Fig. 1g and S5 display the energy dispersive X-ray spectroscopy (EDS) elemental mapping analysis for the (Ni, Fe)OOH@Ni_xP. The Fe and O are uniformly distributed in the (Ni, Fe)OOH nanoparticles and the P is mainly concentrated in the Ni_xP nanorod, while Ni is distributed over the entire (Ni, Fe)OOH@Ni_xP. The above results confirm that the (Ni, Fe)OOH/Ni₁₂P₅/Ni₂P dual-interface is successfully integrated into the (Ni, Fe)OOH@Ni_xP catalyst.

The chemical composition and valence state of the target (Ni, Fe)OOH@Ni_xP, pure (Ni, Fe)OOH, and pure Ni_xP are studied by X-ray photoelectron spectroscopy (XPS). The full XPS spectrum in Fig. 2a reveals the appearance of Ni, Fe, O and P elements in the (Ni, Fe)OOH@Ni_xP, which is in agreement with the results of TEM-EDS mapping. In the Ni 2p_{3/2} spectrum of pure Ni_xP (Fig. 2b), the peak at 853.5 eV corresponds to the formation of Ni-P bonds [29]. Meanwhile, the broad peak at 856.3 eV can be assigned to Ni²⁺, which may result from the inevitable oxidation of metallic Ni in air exposure [18]. The decreased signal of Ni⁰ peak and the increased signal of Ni²⁺ peak can be clearly observed in the Ni 2p_{3/2} spectrum of (Ni, Fe)OOH@Ni_xP, which may be ascribed to formation of the Ni/Fe (oxy)hydroxides nanoparticles on the Ni_xP surface. For the P 2p spectrum of (Ni, Fe)OOH@Ni_xP shown in Fig. 2c, two peaks of P 2p_{3/2} (128.9 eV) and P 2p_{1/2} (130.5 eV) are ascribed to the Ni-P bond, manifesting the formation of Ni phosphide in the (Ni, Fe)OOH@Ni_xP [30]. The broad peak at 133.4 eV is assigned to phosphate species, may play a crucial role for preventing the active sites from chlorine corrosion in seawater [31–33]. The Fe 2p spectrum of (Ni, Fe)OOH@Ni_xP (Fig. 2d) is deconvoluted into



Scheme 1. Schematic illustration for the construction of (Ni, Fe)OOH@Ni_xP catalyst.

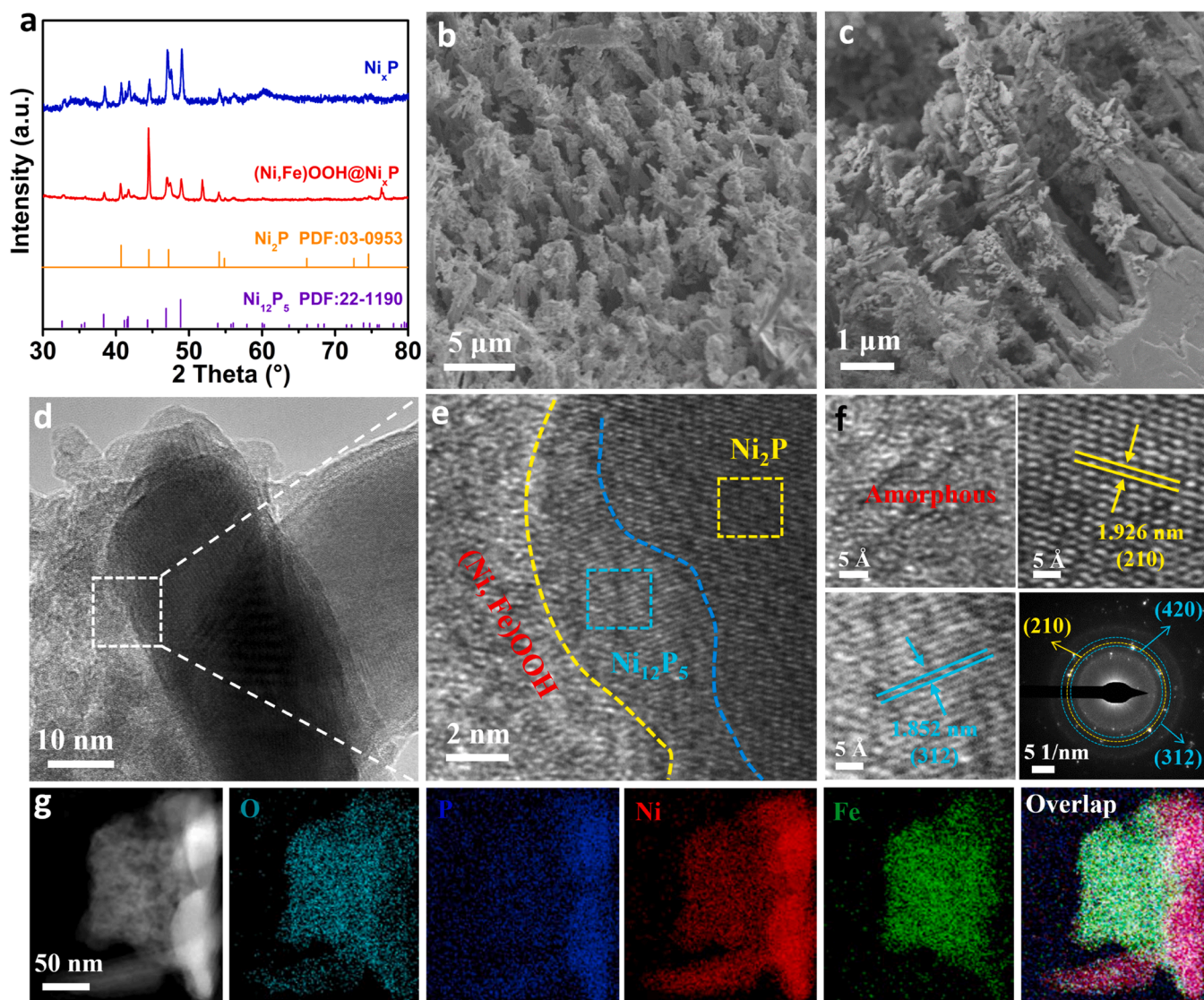


Fig. 1. (a) XRD pattern of the (Ni, Fe)OOH@Ni_xP and Ni_xP catalysts. (b, c) SEM, (d) TEM, (e, f) HRTEM images and the SAED pattern of the (Ni, Fe)OOH@Ni_xP. (g) EDS mapping spectrum of O, P, Ni, and Fe.

four spin-orbit peaks for Fe 2p_{3/2} (711.5 and 714.3 eV) and Fe 2p_{1/2} (725.2 and 728.4 eV), and these peaks are accompanied by their corresponding satellite ones, suggesting the coexistence of Fe²⁺/Fe³⁺ oxidation states [34]. The O 1s spectrum of (Ni, Fe)OOH@Ni_xP in Fig. 2e exhibits two peaks at 530.0 and 531.5 eV assigned to metal-O and metal-OH bonds, respectively [9]. Additionally, the apparent shift of P 2p and Ni 2p peak can be observed in Fig. 2d and e, which could be attributed to the strong electron interaction at the interface, further implying the formation of a strong BEF between Ni/Fe (oxy)hydroxides and Ni phosphide [35]. Raman spectrum of the (Ni, Fe)OOH@Ni_xP in Fig. S6 presents some peaks at 219, 288, 395 and 580 cm⁻¹, corresponding to the (Ni, Fe)OOH phase, which can be also clearly observed in the Raman spectrum of pure (Ni, Fe)OOH [36,37]. Beyond that, the peak located at 478 cm⁻¹ is assigned to the Ni_xP phase, consistent with the Raman result of pure Ni_xP [38]. The above analysis confirms the coexistence of (Ni, Fe)OOH and Ni_xP phases in the (Ni, Fe)OOH@Ni_xP. Fascinatingly, the magnified Raman spectrum of the (Ni, Fe)OOH@Ni_xP in Fig. S7 shows that all the characteristic peaks of (Ni, Fe)OOH phase are blue-shifted relative to that for pure (Ni, Fe)OOH sample, implying the increased electron cloud density around the (Ni, Fe)OOH species in (Ni, Fe)OOH@Ni_xP. Correspondingly, the peak of the Ni_xP phase is red-shifted compared to that for pure Ni_xP sample, suggesting more

electron-deficient Ni_xP species in (Ni, Fe)OOH@Ni_xP [39,40]. This result indicates that electron transfer from Ni_xP to (Ni, Fe)OOH exists in the target (Ni, Fe)OOH@Ni_xP, consistent with the XPS analysis.

It is well known that the mass transfer at solid-liquid interface plays a pivotal role in electrocatalytic process, which is generally reflected by surface wettability of as-fabricated catalysts [41]. In response, the contact angle tests are employed to investigate the wettability. As shown in Fig. 2f, the (Ni, Fe)OOH@Ni_xP exhibits the superhydrophilic property with a near 0° of contact angle (CA). By contrast, bare NF has the inferior hydrophilic property with a large water CA of 86.38°. Additionally, the aerophobic property of the catalysts under the electrolyte is investigated by measuring the CA of the air bubbles in the 1.0 M KOH solution. The bubble CA of the (Ni, Fe)OOH@Ni_xP (133.09°) is higher than that of the bare NF (92.09°), indicating that the (Ni, Fe)OOH@Ni_xP possesses the superaerophobic characteristics [42]. The superhydrophilic and superaerophobic properties are conducive to expediting the electrolyte supplement and the bubbles products escape in the catalyst surface microenvironment, thus facilitating the reaction kinetics during the OER process. It has been reported that the produced gas bubbles generally have the high adhesion force with catalyst surface during the electrochemical OER process, which would lead to the discontinuous

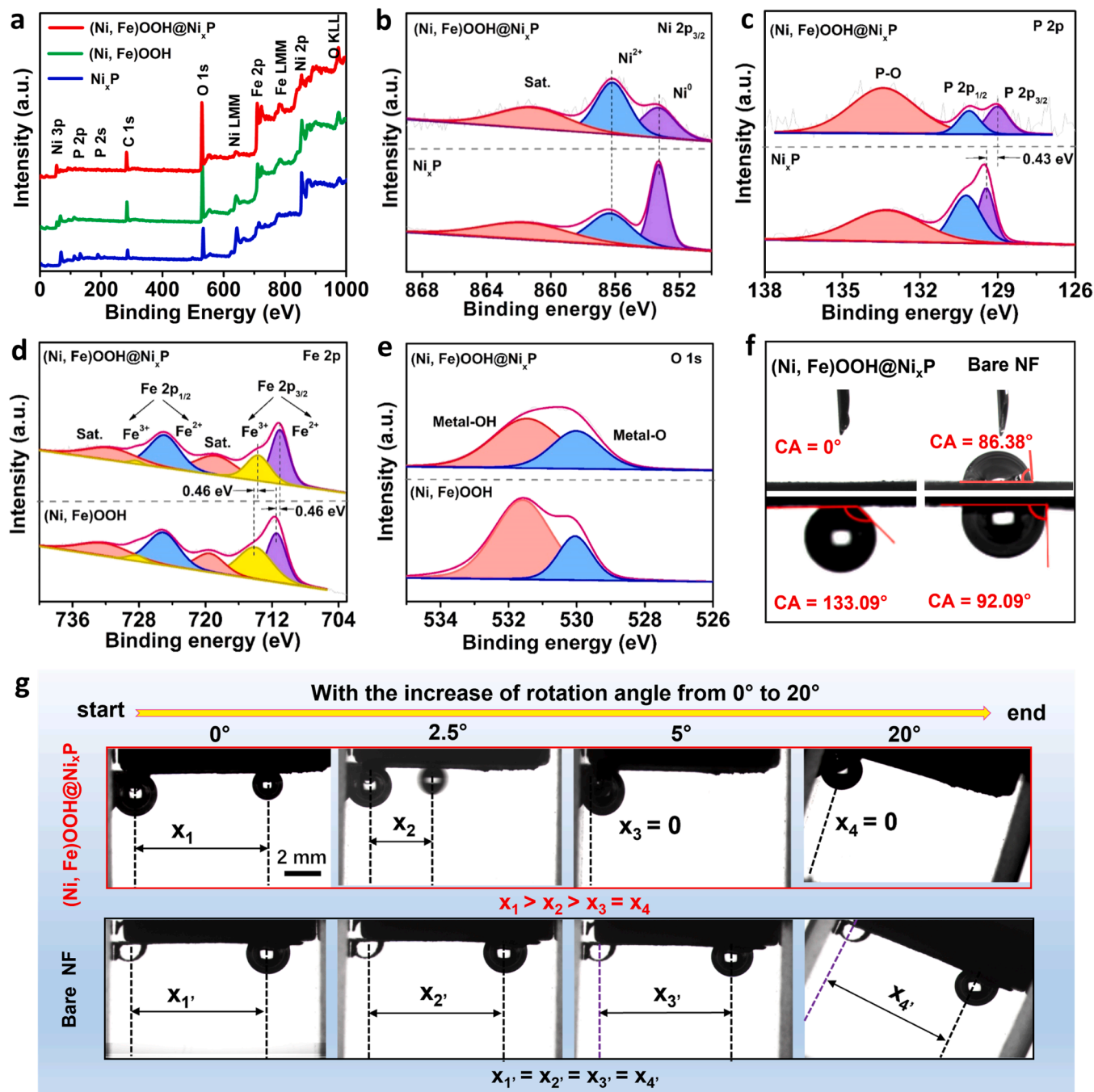


Fig. 2. (a) Full XPS spectra. High-resolution XPS spectra of (b) Ni 2p, (c) P 2p, (d) Fe 2p, and (e) O 1s (f) Droplet contact angle images and air bubble contact angle images. (g) Air bubble slide angle images of the (Ni, Fe)OOH@Ni_xP and bare NF.

solid-liquid contact line and the decrease exposure of active sites [43]. Therefore, the rapid gas bubble detachment on the (Ni, Fe)OOH@Ni_xP surface is of significant to accelerate OER kinetics. As shown in Fig. 2g, the slide angle test shows the large displacement of the air bubble in a tiny inclination angle for the (Ni, Fe)OOH@Ni_xP, demonstrating a negligible adhesive force between the bubble and the catalyst surface [44]. Employing bare NF as contrastive samples, the air bubble firmly adheres to the surface without any detachment during the angle increase from 0° to 20°, manifesting strong adhesive force between NF and bubble [35]. In brief, the unique rod-like nanoarray architecture equipped with numerous nanoparticles on the surface of (Ni, Fe)OOH@Ni_xP could minimize the gas-liquid contact area and accelerate bubble detachment, thus improving the transport efficiency of

electrolyte and gas products.

3.2. Evaluation of electrocatalytic OER performance

The OER performances of the (Ni, Fe)OOH@Ni_xP, (Ni, Fe)OOH, Ni_xP, and commercial RuO₂ are appraised through a standard three-electrode configuration at room temperature. Fig. S8a shows the linear sweep voltammetry (LSV) polarization curves of the prepared catalysts in 1.0 M KOH media. As can be seen, the (Ni, Fe)OOH@Ni_xP requires the ultralow overpotentials of mere 211 and 250 mV to drive the current densities of 100 and 500 mA cm⁻², respectively, which are considerably lower than those of (Ni, Fe)OOH (243 and 283 mV), Ni_xP (301 and 344 mV), RuO₂ (345 and 448 mV), and also recently reported

NiFe-based catalysts (Fig. S8b and Table S1), indicating its remarkable electrocatalytic OER activity. Furthermore, the (Ni, Fe)OOH@Ni_xP has a smaller Tafel slope of 33 mV dec⁻¹ compared to the (Ni, Fe)OOH (42 mV dec⁻¹), Ni_xP (49 mV dec⁻¹) and RuO₂ (86 mV dec⁻¹), suggesting that the (Ni, Fe)OOH@Ni_xP has an optimized OER kinetics (Fig. S8c). To unveil the origins of excellent OER activity, the electrochemical active surface areas (ECSAs) of the (Ni, Fe)OOH@Ni_xP, (Ni, Fe)OOH, and Ni_xP are calculated by evaluating double-layer capacitance (C_{dl}) obtained through performing CV measurements at different scan rates (Fig. S9a-c). As shown in Fig. S8d, the C_{dl} value is calculated to be 9.5 mF cm⁻² for the (Ni, Fe)OOH@Ni_xP, which is approximately 3.7 and 15.8 folds of those for Ni_xP (2.6 mF cm⁻²) and (Ni, Fe)OOH (0.6 mF cm⁻²), respectively, indicating the large active surface area for the (Ni, Fe)OOH@Ni_xP [45]. We also calculate the mass activity of the (Ni, Fe)OOH@Ni_xP, (Ni, Fe)OOH, Ni_xP, and RuO₂ at 270 mV (Fig. S9d). The (Ni, Fe)OOH@Ni_xP exhibits the highest mass activity value of 164.1 A g⁻¹ compared to the (Ni, Fe)OOH (107.2 A g⁻¹), Ni_xP (19.7 A g⁻¹), and RuO₂ (7.8 A g⁻¹), suggesting its improved inherent OER activity. Afterward, catalyst loading has been quantified by calculating the difference in mass before and after synthesis under the various electro-deposition time (Fig. S9e and S9f). Additionally, the charge transport kinetics of the (Ni, Fe)OOH@Ni_xP has been probed by electrochemical impedance spectroscopy (EIS). The Nyquist plots in Fig. S8e

display that the (Ni, Fe)OOH@Ni_xP has a comparatively lower charge transfer resistance (R_{ct}) of 0.85 Ω compared to (Ni, Fe)OOH (1.32 Ω), indicating that the introduction of Ni_xP composition plays a crucial role on boosting the electron transfer for (Ni, Fe)OOH@Ni_xP [46]. Stability has been regarded as another significant metric to assess the OER performance of catalysts. The LSV curves before and after 2000 CV scans are recorded to study cycling durability of the (Ni, Fe)OOH@Ni_xP, in which there is a negligible degradation of the current density (Fig. S8f and Fig. S10), confirming the remarkable cycling stability for the (Ni, Fe)OOH@Ni_xP. The long-term stability is another key index to evaluate the potential application of catalysts, which can be studied by the continuous chronoamperometric test shown in Fig. S8g. Notably, the corresponding curve exhibits a slight fluctuation for a long period (~100 h) at 600 mA cm⁻². Besides, the multi-step chronoamperometric curve of the (Ni, Fe)OOH@Ni_xP is recorded under diverse mutational overpotentials from 226 to 276 mV (Fig. S8h), which shows that the current density remains steady for each stage during the measurement, confirming the extremely remarkable long-term durability for the (Ni, Fe)OOH@Ni_xP.

Seawater, an abundant hydrogen source, has been regarded as ideal alternative for fresh water.[47] The OER performances of above catalysts are first examined in alkaline simulated seawater (1 M KOH + 0.5 M NaCl). As presented in Fig. 3a, the (Ni, Fe)OOH@Ni_xP requires the low overpotentials of 237 and 278 mV to drive the current densities of

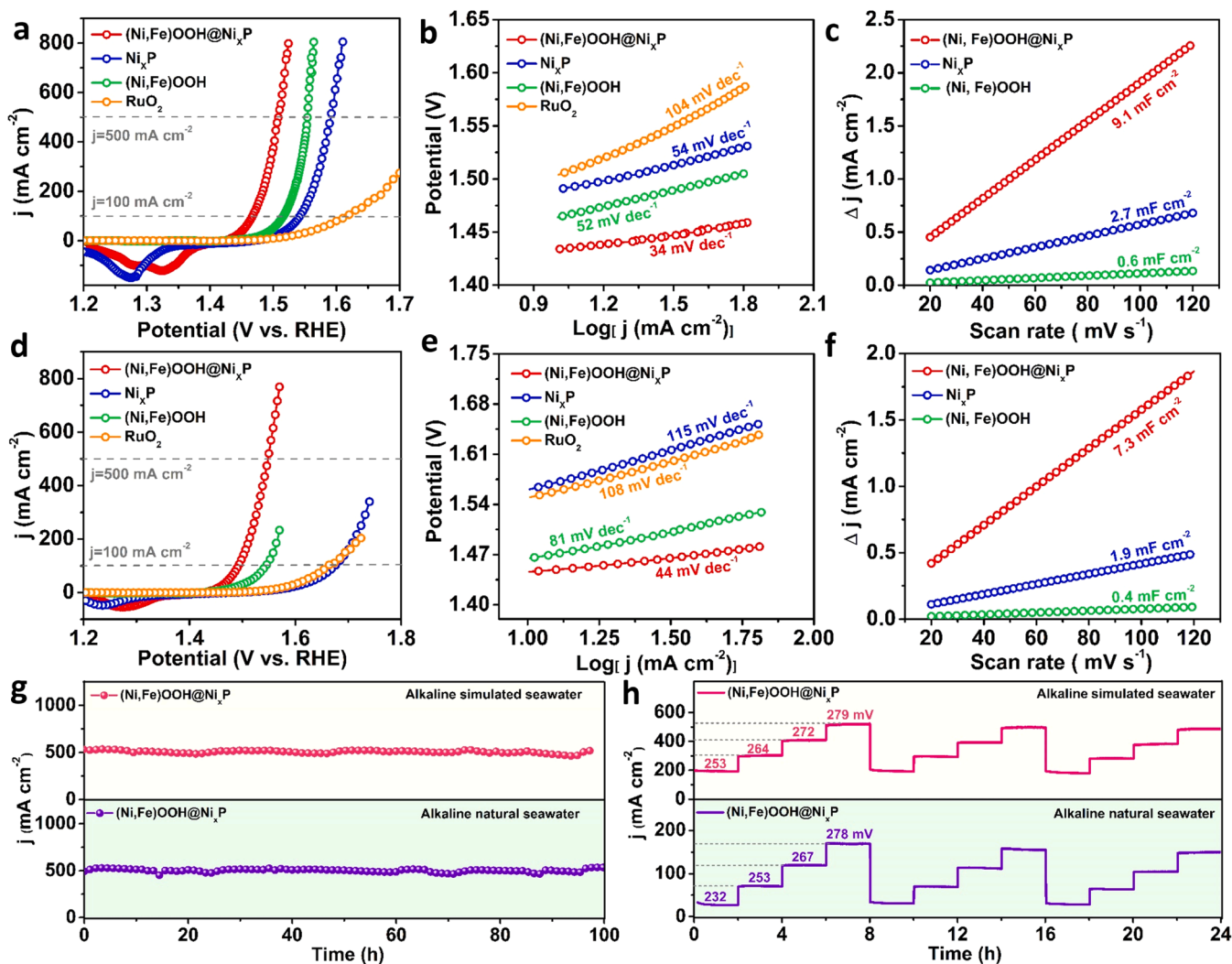


Fig. 3. (a) LSV curves, (b) Tafel plots, and (c) the C_{dl} of the (Ni, Fe)OOH@Ni_xP and contrastive catalysts in alkaline simulated seawater. (d) LSV curves, (e) Tafel plots, and (f) the C_{dl} of the (Ni, Fe)OOH@Ni_xP and contrastive catalysts in alkaline natural seawater. (g) Chronoamperometric curve, and (h) Multi-step chronoamperometric curve for the (Ni, Fe)OOH@Ni_xP.

100 and 500 mA cm⁻² in 1 M KOH + 0.5 M NaCl, respectively, outperforming those of (Ni, Fe)OOH (286 and 324 mV), Ni_xP (312 and 361 mV), and the commercial RuO₂ (η_{100} = 387 mV), demonstrating its excellent OER activity in alkaline simulated seawater. The corresponding Tafel plots in Fig. 3b depict that the (Ni, Fe)OOH@Ni_xP exhibits an extraordinarily lower Tafel slope of 34 mV dec⁻¹ compared to those of Ni_xP (54 mV dec⁻¹), (Ni, Fe)OOH (52 mV dec⁻¹), and commercial RuO₂ (104 mV dec⁻¹), indicating its prominently enhanced OER kinetics. The (Ni, Fe)OOH@Ni_xP has the largest C_{dl} value (9.1 mF cm⁻²) among the investigated three catalysts (Fig. 3c and Fig. S11a-c), suggesting the more exposed active sites on the surface of (Ni, Fe)OOH@Ni_xP. Meanwhile, the (Ni, Fe)OOH@Ni_xP presents the highest mass activity among the Ni_xP, (Ni, Fe)OOH, and commercial RuO₂, suggesting its best inherent OER activity (Fig. S11d). The EIS curves of (Ni, Fe)OOH@Ni_xP and (Ni, Fe)OOH are also recorded in the alkaline simulated seawater (Fig. S12), which show that the (Ni, Fe)OOH@Ni_xP possesses a minimum semicircle diameter in contrast to (Ni, Fe)OOH, indicating its remarkable electronic conductivity.

As shown in Fig. 3d, the OER performances of these catalysts are further evaluated in alkaline natural seawater (1 M KOH + seawater). The (Ni, Fe)OOH@Ni_xP only requires the low overpotentials of 262 and 318 mV to reach the current density of 100 and 500 mA cm⁻² in 1 M KOH + seawater, outperforming the contrast catalysts and other advanced OER catalysts (Table S2). Fig. 3e presents that the (Ni, Fe)OOH@Ni_xP shows the smallest Tafel slope value of 44 mV dec⁻¹ compared to (Ni, Fe)OOH (81 mV dec⁻¹), Ni_xP (115 mV dec⁻¹), and commercial RuO₂ (108 mV dec⁻¹), illustrating its fastest reaction kinetics. It is worth mentioning that the (Ni, Fe)OOH@Ni_xP possesses the highest C_{dl} value of 7.3 mF cm⁻² among all the investigated catalysts (Fig. 3f and S13a-c), confirming that a large number of active sites are exposed on the surface of the (Ni, Fe)OOH@Ni_xP. As presented in Fig. S13d and S14, the (Ni, Fe)OOH@Ni_xP displays a larger mass activity and smaller R_{ct} than the contrast catalysts, suggesting its high intrinsic OER activity and electrical conductivity, respectively. The long-term stability is assessed in both alkaline simulated seawater and natural seawater. The chronoamperometric test indicate that the (Ni, Fe)OOH@Ni_xP could be steadily operated nearly 100 h at large current density of 500 mA cm⁻² (Fig. 3g). Based on the multi-step chronoamperometric measurement results (Fig. 3h), the (Ni, Fe)OOH@Ni_xP also exhibits a remarkable stability at the different potentials. Furthermore, the comparison of LSV curves before and after 2000 cycles confirms the excellent cycling stability of the (Ni, Fe)OOH@Ni_xP (Fig. S15). Such outstanding durability may results from the superior corrosion resistance of (Ni, Fe)OOH@Ni_xP given by the in-situ generated phosphate species during OER in seawater.

After long-term OER stability test in alkaline natural seawater, the chemical components and surface morphology are examined for the (Ni, Fe)OOH@Ni_xP. For the high-resolution XPS spectra of Ni 2p (Fig. S16a), the peak at 852.96 eV originated from Ni_xP species entirely disappears, illustrating that the oxidation of Ni_xP occurs on the surface of (Ni, Fe)OOH@Ni_xP. This could also be verified by observing complete disappearance of P 2p peak and the enhancement of P-O peak from the high-resolution P 2p XPS spectrum (Fig. S16b). In the Fe 2p high-resolution XPS spectrum (Fig. S16c), the peaks attributed to Fe³⁺ at 712.86 (Fe 2p_{3/2}) and 726.76 eV (Fe 2p_{1/2}) display a remarkable increase after OER test, which may result from the oxidation of the Fe species during the OER process [48]. According to the XRD result (Fig. S16d), the characteristic peaks at 38.4, 40.8, 44.6, 46.9, 47.3, and 48.9° exhibits an obvious decline after the OER test, which may be indexed to the partial transformation from the crystalline Ni_xP to amorphous phosphate species during the OER process [5]. SEM and TEM images in Fig. S17a and S17b show that the microstructure of (Ni, Fe)OOH@Ni_xP are well retained after prolonged durability test, verifying its excellent structural stability and high corrosion resistance. The EDS elemental mapping images of (Ni, Fe)OOH@Ni_xP also display the similar distribution of P, O, Ni, and Fe elements as initial ones (Fig. S17c). These results indicate

the excellent morphology and component stability for (Ni, Fe)OOH@Ni_xP.

3.3. Theoretical calculations

The DFT calculations are conducted to uncover the effect of dual-interface on the electronic structure as well as the promotion mechanism toward OER for the (Ni, Fe)OOH@Ni_xP. Fig. S18 displays the optimized atomic models of (Ni, Fe)OOH, (Ni, Fe)OOH@Ni₁₂P₅/Ni₂P, and (Ni, Fe)OOH@Ni₁₂P₅/Ni₂P. As shown in Fig. 4a, the charge density difference analysis indicates that more charge transfer from Ni₁₂P₅ to NiFeOOH in the (Ni, Fe)OOH@Ni₁₂P₅/Ni₂P (2.81 e) than that in the (Ni, Fe)OOH@Ni₁₂P₅ (2.74 e). This result suggests that the presence of Ni₁₂P₅/Ni₂P interface can enhance the charge transfer ability between the (Ni, Fe)OOH and Ni₁₂P₅, thus facilitating the formation of asymmetric charge distribution on them. As known, the charge transfer ability at interface is closely associated with the relative difficulty level of the electron escaping from the hetero-component surface, which can be reflected in work function (WF) [23]. The WF calculations have been performed for the NiFeOOH, Ni₂P, Ni₁₂P₅ and Ni₁₂P₅/Ni₂P, and their values of 5.387, 5.031, 4.825 and 4.652 eV are determined, respectively (Fig. 4b and S19). Compared with that of the NiFeOOH@Ni₁₂P₅ (0.562 eV) and NiFeOOH@Ni₂P (0.356 eV) couples, the relatively larger WF difference value of 0.735 eV between NiFeOOH and Ni₁₂P₅/Ni₂P is beneficial for promoting the interfacial electron transfer and forming the strong BEF (Fig. 4c). The DOS is used to gain insight into the inherent electronic properties and its influence on oxygen intermediate adsorption. As shown in Fig. 4d, the local electron states for the NiFeOOH, NiFeOOH@Ni₁₂P₅, and NiFeOOH@Ni₁₂P₅/Ni₂P reside across the Fermi level, which indicates their metallic feature. These electron states at Fermi level are mainly attributed to the contribution of Ni 3d orbitals. The higher DOS at Fermi level of NiFeOOH@Ni₁₂P₅/Ni₂P than those of NiFeOOH and NiFeOOH@Ni₁₂P₅ indicates the increased electron mobility in NiFeOOH@Ni₁₂P₅/Ni₂P, predicting the rapid electron transport from the catalyst surface toward the adsorbed oxygen species [49]. According to the d-band center theory, the electron density near the Fermi level can affect the binding energy of the reaction intermediate on catalyst surface. As shown in Fig. 4e, the d band center (E_d) of Ni 3d in NiFeOOH@Ni₁₂P₅/Ni₂P is closer to the Fermi level than those in NiFeOOH@Ni₁₂P₅ and NiFeOOH, suggesting a stronger bonding strength with the oxygen intermediates for the fast adsorption kinetics [50]. Gibbs free energy calculation is further investigated to gain insight into the mechanism of the OER process (Fig. 4f and S20), in which four successive elementary reaction steps have been taken into consideration, namely adsorption of OH* on active sites, dehydrogenation to form O* intermediate, OH* adsorbed on the surface with getting OOH* and O₂ generation (second dehydrogenation process). The free energy profiles of above steps at U = 0 are presented in Fig. 4g, in which all the elementary reactions undergo an uphill (endothermic) step. In particular, the rate-determining step (RDS) for both NiFeOOH and NiFeOOH@Ni₁₂P₅ are the second electrochemical step from *OH to *O with an energy barrier of 2.32 and 2.04 eV, respectively, while the RDS for NiFeOOH@Ni₁₂P₅/Ni₂P is altered to the conversion from *O to *OOH with an energy barrier of 1.78 eV (Fig. 4h). These results show that the adsorptions of *OH on NiFeOOH and NiFeOOH@Ni₁₂P₅ are too strong. Introducing the Ni₂P in NiFeOOH@Ni₁₂P₅/Ni₂P to form the dual-interface structure can not only change the RDS of the catalyst, but also decrease the free energy of *OOH formation, thus leading to the superior intrinsic OER activity. At U = 1.23 V, the RDS in NiFeOOH@Ni₁₂P₅/Ni₂P has an energy barrier of 0.55 eV, which is reduced by 0.54 and 0.26 eV compared with that of NiFeOOH and NiFeOOH@Ni₁₂P₅, respectively (Fig. 4i and j), further illustrating the higher OER activity for NiFeOOH@Ni₁₂P₅/Ni₂P. Additionally, DFT calculations are also used to reveal the change of ClOR kinetics after introducing the dual-interface in NiFeOOH@Ni₁₂P₅/Ni₂P. As known, the Cl⁻ adsorption is the first step of ClOR, which plays a vital role in the subsequent

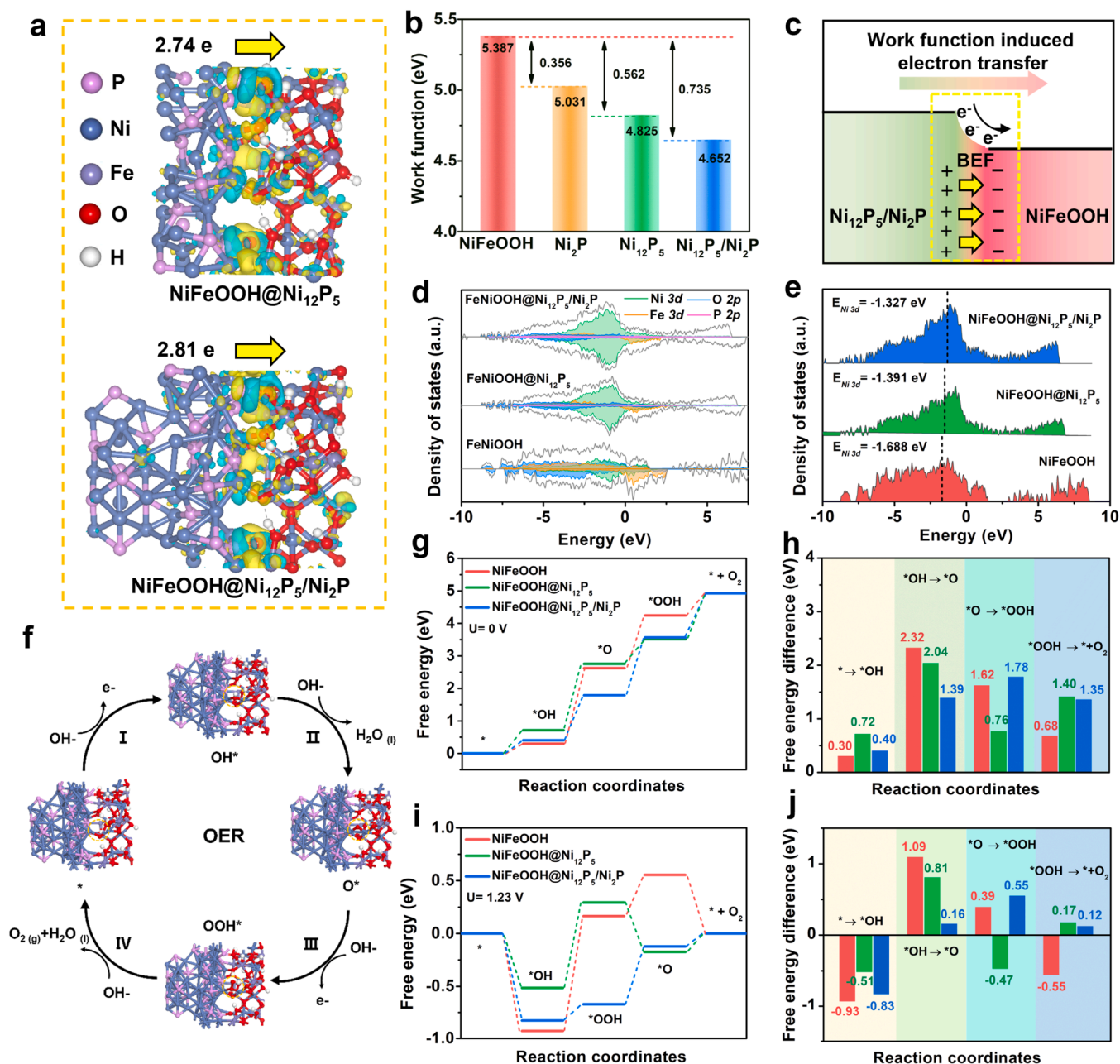


Fig. 4. (a) Charge density difference of the $\text{NiFeOOH@Ni}_{12}\text{P}_5$ and $\text{NiFeOOH@Ni}_{12}\text{P}_5/\text{Ni}_2\text{P}$. (b) Work function values of NiFeOOH , Ni_2P , Ni_{12}P_5 , and $\text{Ni}_{12}\text{P}_5/\text{Ni}_2\text{P}$. (c) Charge transfer process in $\text{NiFeOOH@Ni}_{12}\text{P}_5/\text{Ni}_2\text{P}$. (d) PDOS, and (e) DOS of $\text{NiFeOOH@Ni}_{12}\text{P}_5/\text{Ni}_2\text{P}$, $\text{NiFeOOH@Ni}_{12}\text{P}_5$ and NiFeOOH . (f) The adsorption model of $\text{NiFeOOH@Ni}_{12}\text{P}_5/\text{Ni}_2\text{P}$ in OER process. (g, i) Reaction pathways in the OER process. (h, j) Corresponding free energy difference for $\text{NiFeOOH@Ni}_{12}\text{P}_5/\text{Ni}_2\text{P}$, $\text{NiFeOOH@Ni}_{12}\text{P}_5$ and NiFeOOH .

reaction. Herein, the adsorption energy (E_{ads}) of initial patterns of Cl^- on NiFeOOH , $\text{NiFeOOH@Ni}_{12}\text{P}_5$, and $\text{NiFeOOH@Ni}_{12}\text{P}_5/\text{Ni}_2\text{P}$ are considered, and the corresponding adsorption models are presented in Fig. S21a. As shown in Fig. S21b, the NiFeOOH shows the most negative E_{ads} value of -2.632 eV , suggesting the strong Cl^- adsorption ability on NiFeOOH surface. Notably, the E_{ads} values are decreased to -2.279 and -2.114 eV for $\text{NiFeOOH@Ni}_{12}\text{P}_5$ and $\text{NiFeOOH@Ni}_{12}\text{P}_5/\text{Ni}_2\text{P}$, respectively. That means Cl^- is much harder to be adsorbed on the surface of $\text{NiFeOOH@Ni}_{12}\text{P}_5/\text{Ni}_2\text{P}$, which is good for the exposure of the adsorption sites for oxygen intermediates in the OER process compared with NiFeOOH and $\text{NiFeOOH@Ni}_{12}\text{P}_5$. Collectively, constructing the $\text{NiFeOOH/Ni}_{12}\text{P}_5/\text{Ni}_2\text{P}$ dual-interface to introduce the reinforced BEF in a catalyst could simultaneously reduce the energy barrier of RDS for intrinsically accelerating OER process and weaken the Cl^- adsorption

ability for partly hindering CLOR process, which is beneficial to enhance the catalytic performance for chlorine-free seawater oxidation.

3.4. Evaluation of overall seawater splitting performance

The performance of overall seawater splitting is further investigated by integrating the $(\text{Ni, Fe})\text{OOH@Ni}_x\text{P}$ and Ni_xP into a lab-scale seawater electrolyzer, in which the former is used as the anode for OER and the latter as the cathode for HER (Fig. 5a). As presented in Fig. 5b, the $(\text{Ni, Fe})\text{OOH@Ni}_x\text{P}||\text{Ni}_x\text{P}$ electrolyzer generates the large current densities of 100 and 500 mAcm^{-2} at mere 1.71 and 1.81 V in alkaline natural seawater, respectively, which are significantly better than the control $(\text{Ni, Fe})\text{OOH}||\text{Ni}_x\text{P}$, $\text{Ni}_x\text{P}||\text{Ni}_x\text{P}$, and other recently reported seawater electrolyzers (Fig. 5c and Table S3). The Nyquist plots in Fig. 5d show

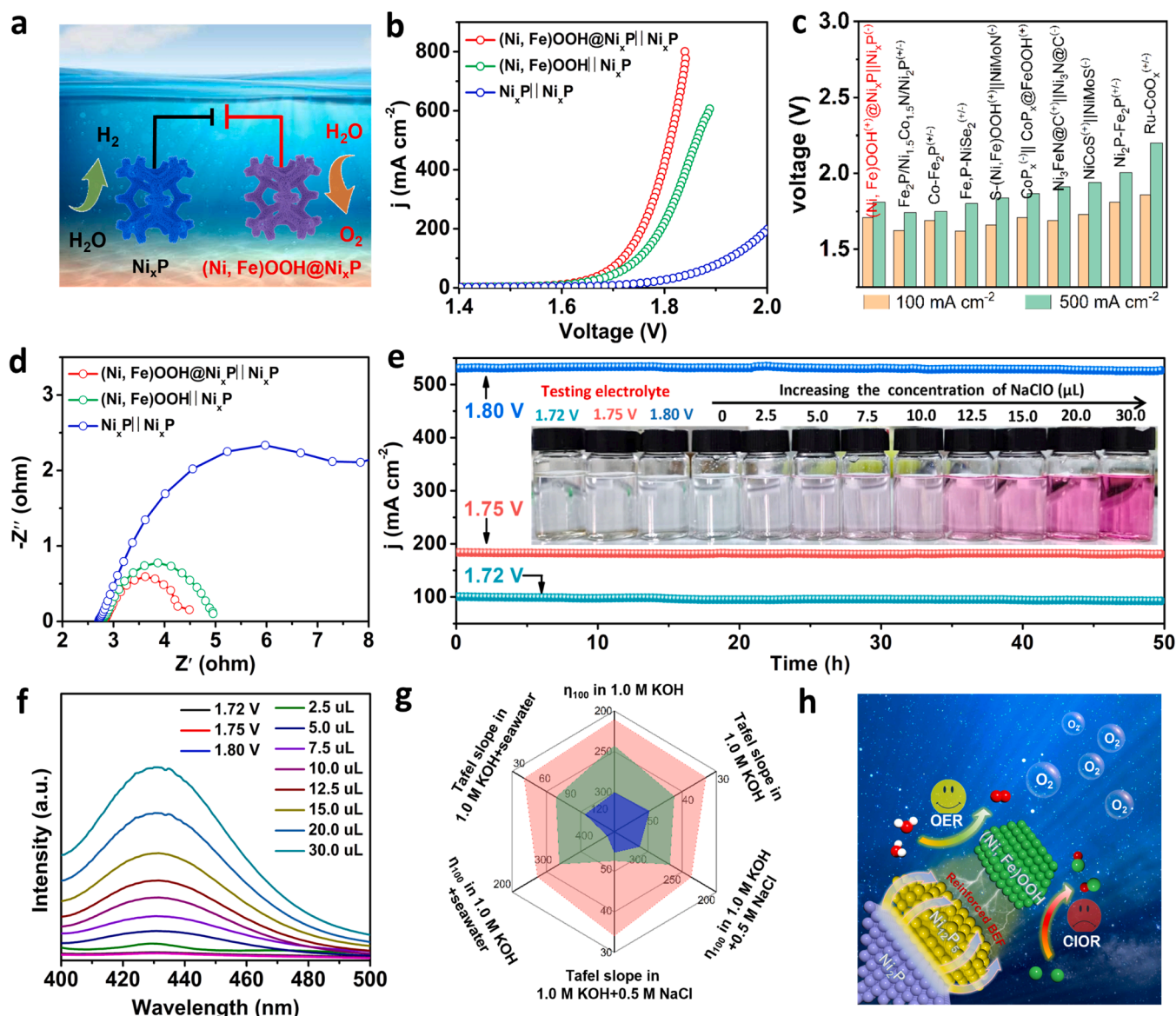


Fig. 5. (a) Schematic illustration of the seawater electrolyzer. (b) LSV curves, and (c) Comparison of the voltages required to achieve the current densities of 100 and 500 mA cm⁻². (d) Nyquist plots of different catalyst electrolyzers. (e) Long-term stability test of the (Ni, Fe)OOH@Ni_xP||Ni_xP electrolyzer performed at potentials of 1.72, 1.75, and 1.80 V, inset: Optical image of the DPD test after long-term stability test. (f) UV-vis absorption spectra of the testing electrolyte. (g) Comprehensive catalytic performance comparison of the (Ni, Fe)OOH@Ni_xP, (Ni, Fe)OOH, and Ni_xP. (h) Schematic charts of performance interpretation for the (Ni, Fe)OOH@Ni_xP.

that the (Ni, Fe)OOH@Ni_xP||Ni_xP electrolyzer has the fastest charge transfer rate. The operating durability is a crucial metric to assess the seawater splitting performance. As presented in Fig. 5e, this (Ni, Fe)OOH@Ni_xP||Ni_xP electrolyzer can retain outstanding catalytic activity with no noticeable degradation over 50 h operation at the cell voltages of 1.72, 1.75, and 1.80 V. Following the long-term stability tests, the color change of electrolyte used under each cell voltage is subsequently examined using N, N-diethyl-p-phenylenediamine (DPD) reagent, in order to determine whether ClO⁻ has been generated in seawater splitting. As can be seen, there is no color change in all testing electrolyte (Figure 5e, inset), indicating that no ClO⁻ formation under the cell voltages of 1.72, 1.75, and 1.80 V, respectively. The corresponding UV-vis absorption spectra results further confirm the above conclusions (Fig. 5f and S22).

Based on the results of above electrochemical measurements, we further evaluate the comprehensive performance of the (Ni, Fe)OOH@Ni_xP, (Ni, Fe)OOH, and Ni_xP catalysts, in which radar chart is built to compare the overpotentials for OER at 100 mA cm⁻² (η_{100}) and

Tafel slope in abovementioned three electrolytes. As known, the closed loop area is proportional to the comprehensive performance, and the larger the better. Obviously, the comprehensive catalytic performance of the (Ni, Fe)OOH@Ni_xP is better than those of the (Ni, Fe)OOH, and Ni_xP (Fig. 5g). Such superior activities of the (Ni, Fe)OOH@Ni_xP can be attributed to the (Ni, Fe)OOH/Ni₁₂P₅/Ni₂P dual-interface: (i) The former (Ni, Fe)OOH/Ni₁₂P₅ interface can create spontaneous BEF by intelligently establishing asymmetric charge redistribution to achieve the adsorption of oxygen intermediates. (ii) The latter Ni₁₂P₅/Ni₂P interface could enhance the electron transfer ability and strengthen the BEF for reducing the energy barrier of RDS (Fig. 5h). (iii) The constructed (Ni, Fe)OOH/Ni₁₂P₅/Ni₂P dual-interface could synergistically weaken the Cl⁻ adsorption ability for partly hindering the ClOR process, thus boosting chlorine-free seawater oxidation.

4. Conclusion

In summary, the (Ni, Fe)OOH@Ni_xP heterostructure consisting of

(Ni, Fe)OOH/Ni₁₂P₅/Ni₂P dual-interface has been successfully prepared as efficient OER catalyst for chlorine-free seawater electrolysis at high current density. Experimental and theoretical results demonstrate that the asymmetric charge redistribution at (Ni, Fe)OOH/Ni₁₂P₅ interface could form a spontaneous BEF, which act as the reaction area to absorb and transform the oxygen intermediates. Meanwhile, the Ni₁₂P₅/Ni₂P interface offers an enhanced intrinsic driving force for promoting electron transfer and strengthening interfacial BEF, which can lower the free energy for the RDS of *O → *OOH. Furthermore, such dual-interface can synergistically endow the catalyst with high energy barrier of Cl⁻ adsorption, which may impede the ClOR process in certain degree. As a result, the (Ni, Fe)OOH@Ni_xP catalyst shows extraordinarily superior OER catalytic performance in alkaline water and seawater, which deliver the large current densities of 500 mA cm⁻² at ultra-low overpotentials of 250, 278, and 318 mV in 1.0 M KOH, 1.0 M KOH + 0.5 M NaCl, and 1.0 M KOH + seawater, respectively. In addition, it remains highly stable for nearly 100 h at the current density of 500 mA cm⁻² in above three electrolytes, indicating the excellent long-term stability. More importantly, the generated hypochlorite has barely been detected in the seawater electrolyte when the operating voltage is higher than the theoretical ClOR potential (≥1.72 V) for a long term. This work is expected to inspire the design of heterogeneous catalyst with dual-interface as well as propel the highly efficient and stable seawater electrolysis at high current density.

CRediT authorship contribution statement

Shucong Zhang: Conceptualization, Methodology, Validation, Investigation, Data curation, Writing – original draft. **Yan Wang:** Investigation, Methodology, Investigation. **Xiaotong Wei:** Investigation, Validation. **Lei Chu:** Methodology, Validation. **Weiqlan Tian:** Data Curation. **Huanlei Wang:** Data curation, Supervision. **Minghua Huang:** Conceptualization, Methodology, Validation, Writing – review & editing, Resources, Supervision.

Declaration of Competing Interest

The authors declare that they have no known competing financial interests or personal relationships that could have appeared to influence the work reported in this paper.

Data Availability

Data will be made available on request.

Acknowledgements

This work was financially supported by the National Natural Science Foundation of China (Nos. 22279124 and 52261145700), the Natural Science Foundation of Shandong Province (No. ZR2020ZD10), and the Fundamental Research Funds for the Central Universities (No. 202262010).

Appendix A. Supporting information

Supplementary data associated with this article can be found in the online version at [doi:10.1016/j.apcatb.2023.122926](https://doi.org/10.1016/j.apcatb.2023.122926).

References

- [1] X. Li, Y. Wang, J. Wang, Y. Da, J. Zhang, L. Li, C. Zhong, Y. Deng, X. Han, W. Hu, Sequential electrodeposition of bifunctional catalytically active structures in MoO₃/Ni-NiO composite electrocatalysts for selective hydrogen and oxygen evolution, *Adv. Mater.* 32 (2020), 2003414, <https://doi.org/10.1002/adma.202003414>.
- [2] F. Dionigi, T. Reier, Z. Pawolek, M. Gliech, P. Strasser, Design criteria, operating conditions, and nickel-iron hydroxide catalyst materials for selective seawater electrolysis, *ChemSusChem* 9 (2016) 962–972, <https://doi.org/10.1002/cssc.201501581>.
- [3] T. Ma, W. Xu, B. Li, X. Chen, J. Zhao, S. Wan, K. Jiang, S. Zhang, Z. Wang, Z. Tian, Z. Lu, L. Chen, The critical role of additive sulfate for stable alkaline seawater oxidation on nickel-based electrodes, *Angew. Chem. Int. Ed.* 60 (2021) 22740–22744, <https://doi.org/10.1002/anie.202110355>.
- [4] J.G. Vos, T.A. Wezendonk, A.W. Jeremiasse, M.T.M. Koper, MnO_x/IrO_x as selective oxygen evolution electrocatalyst in acidic chloride solution, *J. Am. Chem. Soc.* 140 (2018) 10270–10281, <https://doi.org/10.1021/jacs.8b05382>.
- [5] Y. Kuang, M.J. Kenney, Y. Meng, W.H. Hung, Y. Liu, J.E. Huang, R. Prasanna, P. Li, Y. Li, L. Wang, M.C. Lin, M.D. McGehee, X. Sun, H. Dai, Solar-driven, highly sustained splitting of seawater into hydrogen and oxygen fuels, *Proc. Natl. Acad. Sci. USA* 116 (2019) 6624–6629, <https://doi.org/10.1073/pnas.1900556116>.
- [6] D. Liu, H. Ai, J. Li, M. Fang, M. Chen, D. Liu, X. Du, P. Zhou, F. Li, K.H. Lo, Y. Tang, S. Chen, L. Wang, G. Xing, H. Pan, Surface reconstruction and phase transition on vanadium-cobalt-iron trimetal nitrides to form active oxyhydroxide for enhanced electrocatalytic water oxidation, *Adv. Energy Mater.* 10 (2020), 2002464, <https://doi.org/10.1002/aenm.202002464>.
- [7] S. Zhao, Y. Yang, Z. Tang, Insight into structural evolution, active sites, and stability of heterogeneous electrocatalysts, *Angew. Chem. Int. Ed.* 61 (2022), e202110186, <https://doi.org/10.1002/anie.202110186>.
- [8] L. Tan, J. Yu, C. Wang, H. Wang, S. Liu, H. Gao, L. Xin, D. Liu, W. Hou, T. Zhan, Partial sulfidation strategy to NiFe-LDH@FeNi₂S₄ heterostructure enable high-performance water/seawater oxidation, *Adv. Funct. Mater.* 32 (2022), 2200951, <https://doi.org/10.1002/adfm.202200951>.
- [9] C. Liang, P. Zou, A. Nairan, Y. Zhang, J. Liu, K. Liu, S. Hu, F. Kang, H.J. Fan, C. Yang, Exceptional performance of hierarchical Ni-Fe oxyhydroxide@NiFe alloy nanowire array electrocatalysts for large current density water splitting, *Energy Environ. Sci.* 13 (2020) 86–95, <https://doi.org/10.1039/C9EE02388G>.
- [10] Y. Huang, L. Hu, R. Liu, Y. Hu, T. Xiong, W. Qiu, M. Balogun, A. Pan, Y. Tong, Nitrogen treatment generates tunable nanohybridization of Ni₂P₃ nanosheets with nickel hydroxide for efficient hydrogen production in alkaline, seawater and acidic media, *Appl. Catal. B Environ.* 251 (2019) 181–194, <https://doi.org/10.1016/j.apcatb.2019.03.037>.
- [11] Y. Zhang, L. You, Q. Liu, Y. Li, T. Li, Z. Xue, G. Li, Interfacial charge transfer in a hierarchical Ni₂P/FeOOH heterojunction facilitates electrocatalytic oxygen evolution, *ACS Appl. Mater. Interfaces* 13 (2021) 2765–2771, <https://doi.org/10.1021/acsami.0c20204>.
- [12] S. Niu, W.J. Jiang, T. Tang, L.P. Yuan, H. Luo, J.S. Hu, Autogenous growth of hierarchical NiFe(OH)_x/FeS nanosheet-on-microsheet arrays for synergistically enhanced high-output water oxidation, *Adv. Funct. Mater.* 29 (2019), 1902180, <https://doi.org/10.1002/adfm.201902180>.
- [13] H. Zhang, C. Chen, X. Wu, C. Lv, Y. Lv, J. Guo, D. Jia, Synergistic incorporating RuO₂ and NiFeOOH layers onto Ni₃S₂ nanoflakes with modulated electron structure for efficient water splitting, *Small Methods* 6 (2022), 2200483, <https://doi.org/10.1002/smt.202200483>.
- [14] D. Chen, R. Lu, R. Yu, Y. Dai, H. Zhao, D. Wu, P. Wang, J. Zhu, Z. Pu, L. Chen, J. Yu, S. Mu, Work-function-induced interfacial built-in electric fields in Os-OsSe₂ heterostructures for active acidic and alkaline hydrogen evolution, *Angew. Chem. Int. Ed.* 61 (2022), e202208642, <https://doi.org/10.1002/anie.202208642>.
- [15] L. Zhai, X. She, L. Zhuang, Y. Li, R. Ding, X. Guo, Y. Zhang, Y. Zhu, K. Xu, H.J. Fan, S.P. Lau, Modulating built-in electric field via variable oxygen affinity for robust hydrogen evolution reaction in neutral media, *Angew. Chem. Int. Ed.* 134 (2022), e202116057, <https://doi.org/10.1002/anie.202116057>.
- [16] H. Wang, Y. Wei, G. Wang, Y. Pu, L. Yuan, C. Liu, Q. Wang, Y. Zhang, H. Wu, Selective nitridation crafted a high-density, carbon-free heterostructure host with built-in electric field for enhanced energy density Li-S batteries, *Adv. Sci.* 9 (2022), 2201823, <https://doi.org/10.1002/advs.202201823>.
- [17] J. Li, M. Song, Y. Hu, C. Zhang, W. Liu, X. Huang, J. Zhang, Y. Zhu, J. Zhang, D. Wang, A self-supported heterogeneous bimetallic phosphide array electrode enables efficient hydrogen evolution from saline water splitting, *Nano Res.* (2022), <https://doi.org/10.1007/s12274-022-4608-8>.
- [18] L. Wu, L. Yu, F. Zhang, B. McElhenny, D. Luo, A. Karim, S. Chen, Z. Ren, Heterogeneous bimetallic phosphide Ni₂P-Fe₂P as an efficient bifunctional catalyst for water/seawater splitting, *Adv. Funct. Mater.* 31 (2020), 2006484, <https://doi.org/10.1002/adfm.202006484>.
- [19] W. Xu, G. Fan, S. Zhu, Y. Liang, Z. Cui, Z. Li, H. Jiang, S. Wu, F. Cheng, Electronic structure modulation of nanoporous cobalt phosphide by carbon doping for alkaline hydrogen evolution reaction, *Adv. Funct. Mater.* 31 (2021), 2107333, <https://doi.org/10.1002/adfm.202107333>.
- [20] A. Kumar, V.Q. Bui, J. Lee, A.R. Jadhav, Y. Hwang, M.G. Kim, Y. Kawazoe, H. Lee, Modulating interfacial charge density of NiP₂-FeP₂ via coupling with metallic Cu for accelerating alkaline hydrogen evolution, *ACS Energy Lett.* 6 (2021) 354–363, <https://doi.org/10.1021/acseenergylett.0c02498>.
- [21] Q. Lv, J. Han, X. Tan, W. Wang, L. Cao, B. Dong, Featherlike NiCoP holey nanoarrays for efficient and stable seawater splitting, *ACS Appl. Energy Mater.* 2 (2019) 3910–3917, <https://doi.org/10.1021/acsaem.9b00599>.
- [22] S. Zhang, C. Tan, R. Yan, X. Zou, F.-L. Hu, Y. Mi, C. Yan, S. Zhao, Constructing built-in electric field in heterogeneous nanowire arrays for efficient overall water electrolysis, *Angew. Chem. Int. Ed.* (2023), <https://doi.org/10.1002/anie.202302795>.
- [23] D. Chen, R. Lu, R. Yu, Y. Dai, H. Zhao, D. Wu, P. Wang, J. Zhu, Z. Pu, L. Chen, J. Yu, S. Mu, Work-function-induced interfacial built-in electric fields in Os-OsSe₂ heterostructures for active acidic and alkaline hydrogen evolution, *Angew. Chem. Int. Ed.* 61 (2022), e202208642, <https://doi.org/10.1002/anie.202208642>.

- [24] H. Liu, R. Xie, Y. Luo, Z. Cui, Q. Yu, Z. Gao, Z. Zhang, F. Yang, X. Kang, S. Ge, S. Li, X. Gao, G. Chai, L. Liu, B. Liu, Dual interfacial engineering of a Chevrel phase electrode material for stable hydrogen evolution at 2500 mA cm^{-2} , *Nat. Commun.* 13 (2022) 6382, <https://doi.org/10.1038/s41467-022-34121-y>.
- [25] P. Zhou, L. Tao, S. Tao, Y. Li, D. Wang, X. Dong, T. Fraunheim, X. Fu, X. Lv, S. Wang, Construction of nickel-based dual heterointerfaces towards accelerated alkaline hydrogen evolution via boosting multi-step elementary reaction, *Adv. Funct. Mater.* 31 (2021), 2104827, <https://doi.org/10.1002/adfm.202104827>.
- [26] G. Li, T. Sun, H.-J. Niu, Y. Yan, T. Liu, S. Jiang, Q. Yang, W. Zhou, L. Guo, Triple interface optimization of Ru-based electrocatalyst with enhanced activity and stability for hydrogen evolution reaction, *Adv. Funct. Mater.* 33 (2023), 2212514, <https://doi.org/10.1002/adfm.202212514>.
- [27] X. Xu, T. Guo, J. Xia, B. Zhao, G. Su, H. Wang, M. Huang, A. Toghan, Modulation of the crystalline/amorphous interface engineering on Ni-P-O-based catalysts for boosting urea electrolysis at large current densities, *Chem. Eng. J.* 425 (2021), 130514, <https://doi.org/10.1016/j.cej.2021.130514>.
- [28] H. Han, H. Choi, S. Mhin, Y.R. Hong, K.M. Kim, J. Kwon, G. Ali, K.Y. Chung, M. Je, H.N. Umh, D.H. Lim, K. Davey, S.Z. Qiao, U. Paik, T. Song, Advantageous crystalline-amorphous phase boundary for enhanced electrochemical water oxidation, *Energy Environ. Sci.* 12 (2019) 2443, <https://doi.org/10.1039/C9EE00950G>.
- [29] T. Liu, A. Li, C. Wang, W. Zhou, S. Liu, L. Guo, Interfacial electron transfer of Ni_2P - NiP_2 polymorphs inducing enhanced electrochemical properties, *Adv. Mater.* 30 (2018), e1803590, <https://doi.org/10.1002/adma.201803590>.
- [30] I.K. Mishra, H. Zhou, J. Sun, F. Qin, K. Dahal, J. Bao, S. Chen, Z. Ren, Hierarchical $\text{CoP/Ni}_3\text{P}_4/\text{CoP}$ microsheet arrays as a robust pH-universal electrocatalyst for efficient hydrogen generation, *Energy Environ. Sci.* 11 (2018) 2246–2252, <https://doi.org/10.1039/C8EE01270A>.
- [31] J. Chang, G. Wang, Z. Yang, B. Li, Q. Wang, R. Kuliev, N. Orlovskaya, M. Gu, Y. Du, G. Wang, Y. Yang, Dual-doping and synergism toward high-performance seawater electrolysis, *Adv. Mater.* 33 (2021), 2101425, <https://doi.org/10.1002/adma.202101425>.
- [32] B. Zhang, S. Liu, S. Zhang, Y. Cao, H. Wang, C. Han, J. Sun, High corrosion resistance of NiFe-layered double hydroxide catalyst for stable seawater electrolysis promoted by phosphate intercalation, *Small* 18 (2022), 2203852, <https://doi.org/10.1002/sml.202203852>.
- [33] T. Li, X. Zhao, M.G. Sendek, X. Zhang, L. Xu, Z. Wang, S. Wan, X. Duan, H. Li, W. Liu, D. Zhou, H. Xu, Y. Kuang, X. Sun, Phosphate-decorated $\text{Ni}_3\text{Fe-LDHs@CoP}_x$ nanoarray for near-neutral seawater splitting, *Chem. Eng. J.* 460 (2023), 141413, <https://doi.org/10.1016/j.cej.2023.141413>.
- [34] M.P. Suryawanshi, U.V. Ghorpade, S.W. Shin, U.P. Suryawanshi, E. Jo, J.H. Kim, Hierarchically coupled Ni:FeOOH Nanosheets on 3D N-doped graphite foam as self-supported electrocatalysts for efficient and durable water oxidation, *ACS Catal.* 9 (2019) 5025–5034, <https://doi.org/10.1021/acscatal.9b00492>.
- [35] S. Zhang, W. Wang, F. Hu, Y. Mi, S. Wang, Y. Liu, X. Ai, J. Fang, H. Li, T. Zhai, 2D CoOOH sheet-encapsulated Ni_2P into tubular arrays realizing 1000 mA cm^{-2} -level-current-density hydrogen evolution over 100h in neutral water, *Nano-Micro Lett.* 12 (2020) 140, <https://doi.org/10.1007/s40820-020-00476-4>.
- [36] S. Niu, W.J. Jiang, Z. Wei, T. Tang, J. Ma, J.S. Hu, L.J. Wan, Se-doping activates FeOOH for cost-effective and efficient electrochemical water oxidation, *J. Am. Chem. Soc.* 141 (2019) 7005–7013, <https://doi.org/10.1021/jacs.9b01214>.
- [37] Q. Wen, K. Yang, D. Huang, G. Cheng, X. Ai, Y. Liu, J. Fang, H. Li, L. Yu, T. Zhai, Schottky heterojunction nanosheet array achieving high-current-density oxygen evolution for industrial water splitting electrolyzers, *Adv. Energy Mater.* 11 (2021), 2102353, <https://doi.org/10.1002/aenm.202102353>.
- [38] S. Han, C. Wang, Y. Shi, C. Liu, Y. Yu, S. Lu, B. Zhang, Membrane-free selective oxidation of thioethers with water over a nickel phosphide nanocube electrode, *Cell Rep. Phys. Sci.* 2 (2021), 100462, <https://doi.org/10.1016/j.xcrp.2021.100462>.
- [39] Z. Sun, Y. Wang, L. Zhang, H. Wu, Y. Jin, Y. Li, Y. Shi, T. Zhu, H. Mao, J. Liu, C. Xiao, S. Ding, Simultaneously realizing rapid electron transfer and mass transport in Jellyfish-like Mott-Schottky nanoreactors for oxygen reduction reaction, *Adv. Funct. Mater.* 30 (2020), 1910482, <https://doi.org/10.1002/adfm.201910482>.
- [40] X. Wang, G. Zhan, Y. Wang, Y. Zhang, J. Zhou, R. Xu, H. Gai, H. Wang, H. Jiang, M. Huang, Engineering core-shell $\text{Co}_9\text{S}_8/\text{Co}$ nanoparticles on reduced graphene oxide: efficient bifunctional Mott-Schottky electrocatalysts in neutral rechargeable Zn-Air batteries, *J. Energy Chem.* 68 (2022) 113–123, <https://doi.org/10.1016/j.jechem.2021.09.014>.
- [41] W. Xu, Z. Lu, X. Sun, L. Jiang, X. Duan, Superwetting electrodes for gas-involving electrocatalysis, *Acc. Chem. Res.* 51 (2018) 1590–1598, <https://doi.org/10.1021/acs.accounts.8b00070>.
- [42] K. Tang, H. Hu, Y. Xiong, L. Chen, J. Zhang, C. Yuan, M. Wu, Hydrophobization engineering of the air-cathode catalyst for improved oxygen diffusion towards efficient zinc-air batteries, *Angew. Chem. Int. Ed.* 61 (2022), e202202671, <https://doi.org/10.1002/anie.202202671>.
- [43] M. Bae, Y. Kang, D.W. Lee, D. Jeon, J. Ryu, Superaerophobic polyethyleneimine hydrogels for improving electrochemical hydrogen production by promoting bubble detachment, *Adv. Energy Mater.* 12 (2022), 2201452, <https://doi.org/10.1002/aenm.202201452>.
- [44] H. Yao, X. Wang, K. Li, C. Li, C. Zhang, J. Zhou, Z. Cao, H. Wang, M. Gu, M. Huang, H. Jiang, Strong electronic coupling between ruthenium single atoms and ultrafine nanoclusters enables economical and effective hydrogen production, *Appl. Catal. B Environ.* 312 (2022), 121378, <https://doi.org/10.1002/adfm.202102066>.
- [45] Y. Teng, X.D. Wang, J.F. Liao, W.G. Li, H.Y. Chen, Y.J. Dong, D.B. Kuang, Atomically thin defect-rich Fe-Mn-O hybrid nanosheets as high efficient electrocatalyst for water oxidation, *Adv. Funct. Mater.* 28 (2018), 1802463, <https://doi.org/10.1002/adfm.201802463>.
- [46] J. Zhou, Z. Han, X. Wang, H. Gai, Z. Chen, T. Guo, X. Hou, L. Xu, X. Hu, M. Huang, S.V. Levchenko, H. Jiang, Discovery of quantitative electronic structure-OER activity relationship in metal-organic framework electrocatalysts using an integrated theoretical-experimental approach, *Adv. Funct. Mater.* 31 (2021), 2102066, <https://doi.org/10.1002/adfm.202102066>.
- [47] S. Dresch, F. Dionigi, M. Klingenhof, P. Strasser, Direct electrolytic splitting of seawater: opportunities and challenges, *ACS Energy Lett.* 4 (2019) 933–942, <https://doi.org/10.1021/acscenergylett.9b00220>.
- [48] L. Yu, L. Wu, B. McElhenny, S. Song, D. Luo, F. Zhang, Y. Yu, S. Chen, Z. Ren, Ultrafast room-temperature synthesis of porous S-doped Ni/Fe (oxy)hydroxide electrodes for oxygen evolution catalysis in seawater splitting, *Energy Environ. Sci.* 13 (2020) 3439–3446, <https://doi.org/10.1039/D0EE00921K>.
- [49] L. Zhang, W. Cai, N. Bao, Top-level design strategy to construct an advanced high-entropy Co-Cu-Fe-Mo (oxy)hydroxide electrocatalyst for the oxygen evolution reaction, *Adv. Mater.* 33 (2021), 2100745, <https://doi.org/10.1002/adma.202100745>.
- [50] C. Yan, Y.-L. Liu, Q. Zeng, G.-G. Wang, J.-C. Han, 2D nanomaterial supported single-metal atoms for heterogeneous photo/electrocatalysis, *Adv. Funct. Mater.* 33 (2023), 2210837, <https://doi.org/10.1002/adfm.202210837>.